

A Model for Energy Buildup and Eruption Onset in Coronal Mass Ejections

J. T. DAHLIN,^{1,*} S. K. ANTIOCHOS,¹ AND C. R. DEVORE¹

¹*Heliophysics Science Division, NASA Goddard Space Flight Center, Greenbelt, Maryland 20771*

(Received October 3, 2019; Revised October 3, 2019; Accepted October 3, 2019)

Submitted to ApJ

ABSTRACT

Coronal mass ejections (CMEs) and eruptive flares (EFs) are the most energetic explosions in the solar system. Their underlying origin is the free energy that builds up slowly in the sheared magnetic field of a filament channel. We report the first end-to-end numerical simulation of a CME/EF, from zero-free-energy initial state through filament-channel formation to violent eruption, driven solely by the magnetic-helicity condensation process. Helicity is the topological measure of linkages between magnetic flux systems, and is conserved in the corona, building up inexorably until it is ejected into interplanetary space. Numerous investigations have demonstrated that helicity injected by small-scale vortical motions, such as those observed in the photosphere, undergoes an inverse cascade from small scales to large, “condensing” at magnetic-polarity boundaries. Our new results verify that this process forms a filament channel within a compact bipolar region embedded in a background dipole field, and show for the first time that a fast CME eventually occurs via the magnetic-breakout mechanism. We further show that the trigger for explosive eruption is reconnection onset in the flare current sheet that develops above the polarity inversion line: this reconnection forms flare loops below the sheet and a CME flux rope above, and initiates high-speed outward flow of the CME. Our findings have important implications for magnetic self-organization and explosive behavior in solar and other astrophysical plasmas, and for understanding and predicting explosive solar activity.

Keywords: Sun: coronal mass ejections (CMEs), Sun: corona — Sun: magnetic fields — Sun: flares — Sun: filaments, prominences — magnetic reconnection

1. INTRODUCTION

Coronal mass ejections (CMEs) are spectacular manifestations of solar activity in which enormous quantities of plasma and magnetic flux are expelled from the solar atmosphere into interplanetary space. Although they have been studied for decades, the mechanisms governing the gradual energy buildup and explosive release that characterize all CMEs remain subjects of intense investigation, due primarily to the lack of accurate quantitative measurements of the magnetic field in the corona. The many studies, however, have confirmed that all CMEs and flares are associated with solar filament channels (Gaizauskas 1998; Martin 1998), which consist of highly sheared magnetic field localized around polarity inversion lines (PILs) of the radial component of the photospheric magnetic field. This sheared flux is believed to provide the free energy that powers the events. Understanding the energy buildup mechanism leading to explosive eruption, therefore, comes down to understanding how filament channels form.

Although filaments form over all PILs, in quiet Sun as well as active regions, and have been observed for many decades, their origin is still under debate. It is well known, however, that these structures represent a balance of forces between the outward magnetic pressure of the low-lying, strongly sheared flux and the inward magnetic tension of the overlying, mostly unsheared flux. CMEs are believed to be due to the catastrophic disruption of this force balance inherent in all filament channels (see Forbes et al. 2006, and references therein). As a result of the disruption, the

free magnetic energy stored in the corona is rapidly converted into bulk kinetic and thermal energy of the plasma and nonthermal accelerated particles. A twisted flux rope is ejected into the heliosphere, and hot X-ray emitting loops form *via* flare reconnection below the ejection. A central point of controversy is the issue of cause and effect: is the flux rope formed prior to the eruption, and does its ideal destabilization and attendant outward motion induce the flare reconnection as a secondary phenomenon (e.g. Fan 2001; Linker et al. 2003; Kliem & Török 2006)? Or is reconnection the primary actor in both the creation and fast expulsion of the flux rope (as in Antiochos 1998; Antiochos et al. 1999; Moore et al. 2001; DeVore & Antiochos 2008; Karpen et al. 2012; Wyper et al. 2018)? The answers to these questions are fundamental for understanding the mechanism for explosive solar eruptions across all scales (Wyper et al. 2017, and references therein).

The recently developed theory of helicity condensation (Antiochos 2013) proposes an answer to the question of filament channel formation or, equivalently, the mechanism for energy buildup. This theory posits that the photospheric convective motions responsible for coronal heating continually inject magnetic twist/stress into the corona at small scales, and that this twist subsequently is transported by magnetic reconnection to collect at the boundaries of coronal flux systems (PILs) at large scales. Magnetic helicity is a topological measure of flux linkages in magnetized plasmas (Berger & Field 1984; Finn & Antonsen 1985). It is rigorously conserved under ideal motion and is well preserved during reconnection in highly conducting environments such as the corona (Berger 1984). This conservation property implies that the helicity associated with the injected small-scale twist/stress must accumulate in the corona because it cannot be dissipated away locally. Detailed numerical simulations (Zhao et al. 2015; Knizhnik et al. 2015, 2017a,b, 2018) have confirmed the essential features of the process described by Antiochos (2013) and demonstrated that the helicity indeed “condenses” at PILs to form stable magnetic structures whose properties are consistent with those of observed filament channels. A statistically averaged approximation to the full helicity-condensation process has been used by Mackay et al. (2014, 2018) to investigate the formation of filament channels across the full Sun and over multiple solar rotation periods.

The previously cited detailed numerical simulations of helicity injection, transport, and condensation were performed for a closed Cartesian domain and a purely bipolar magnetic field. Eruption was not possible in these cases, because the upper boundary imparted an artificial confinement. These studies, therefore, could not address the issue of the mechanism for force-balance disruption, i.e., eruption onset. In this article, we report the first numerical simulation of helicity condensation in a fully 3D spherical system that realistically captures the structure and dynamics of actual CMEs. The domain extends out to 30 solar radii, so that the upper boundary has no effect on eruption onset. Furthermore, we assume for the magnetic topology a localized bipole, representative of a simple active region, embedded in a background global dipole field. As described in detail below, we find that this simulation captures, for the first time, the self-consistent filament channel formation via helicity condensation together with the explosive eruption that characterizes CMEs. Furthermore, we find that the eruption is driven by magnetic reconnection, rather than by an ideal instability.

2. NUMERICAL MODEL

Our numerical simulation was performed with the Adaptively Refined Magnetohydrodynamics Solver (ARMS; DeVore & Antiochos 2008), which has been used to model both CMEs/eruptive flares (see also Lynch et al. 2008, 2009; Karpen et al. 2012; Masson et al. 2013; Lynch et al. 2016) and the formation of filament channels (Zhao et al. 2015; Knizhnik et al. 2015, 2017a,b, 2018). The magnetic field configuration shown in Figure 1a,b consists of a potential bipolar active region centered at 22.5° N latitude with peak field strength $|B_r| \approx 50$ G (adapted from DeVore & Antiochos 2008) embedded in a background dipole field of strength 10 G. The resulting topology is that of the well-known embedded biopole with its separatrix dome and a pair of spine lines emanating from a 3D null point (Antiochos 1990; Lau & Finn 1990; Priest & Titov 1996). A region of maximally refined grid enclosed the coronal null point, the entire separatrix dome below the null, and a substantial additional volume above the null, in order to resolve the small-scale reconnection dynamics of the helicity-condensation process (Fig. 1b). The initial atmosphere was a spherically symmetric hydrostatic equilibrium with an inverse- r temperature profile at a base temperature $T_s = 2 \times 10^6$ K and pressure $P_s = 4 \times 10^{-1}$ dyn cm $^{-2}$ (adapted from Karpen et al. 2012). We solved the ideal MHD equations with an adiabatic temperature equation (as in DeVore & Antiochos 2008; Karpen et al. 2012). The domain extents were $r \in [1R_s, 30R_s]$, $\theta \in [\pi/16, 15\pi/16]$, and $\phi \in [-\pi, +\pi]$.

This system was energized by motions at the bottom photospheric boundary consisting of 107 close-packed, vortical, B_r -conserving cellular flows within the black-shaded, minority-polarity region (see Fig. 1c). The flows were subsonic

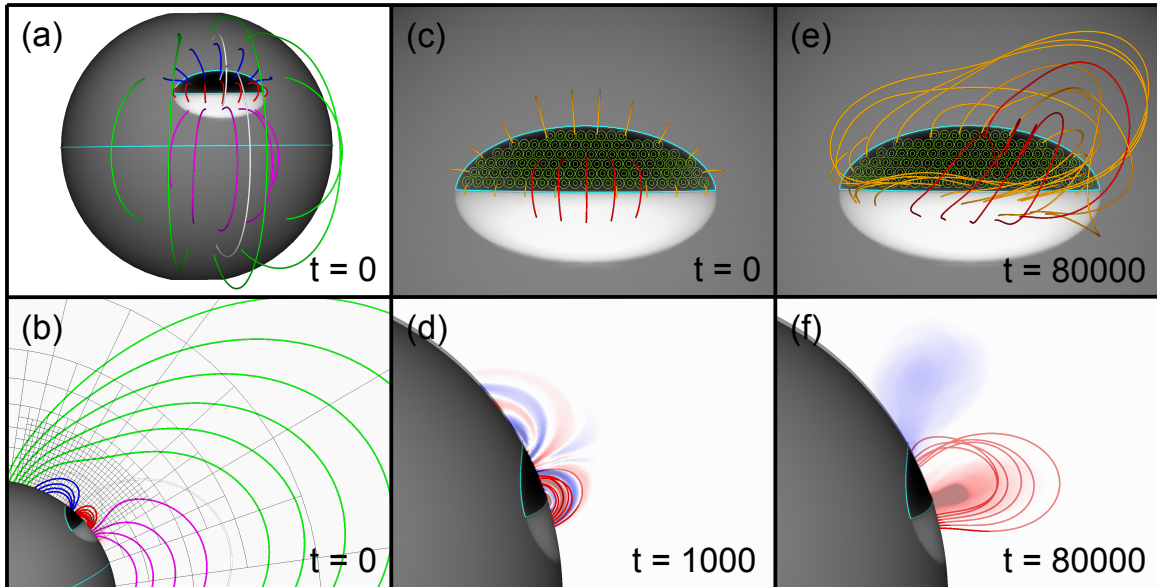


Figure 1. Initial configuration (a,b) and filament-channel formation (c-f) at the indicated times t . Black (white) surface shading indicates minority (majority) magnetic polarity; cyan curves are the surface PILs. Green, blue, red, and magenta field lines illustrate different flux systems in the multipolar topology. Green annuli (c,e) are contours of constant $|\mathbf{v}|$ in the vortical flows, and orange field lines represent low-lying sheared flux above the PIL. Color shading in the $\phi = 0$ plane (d,f) contours the azimuthal field component, B_ϕ , saturated at (d) ± 2 G and (f) ± 30 G. An animation of panels (c,e) and (d,f) is available. The video starts at $t = 0$ and ends at $t = 80000$. Its duration is 5 seconds.

and sub-Alfvénic, attaining a maximum speed $|V_\perp| \approx 50 \text{ km s}^{-1}$ after an initial sinusoidal ramp-up interval 1,000 s in duration. Note that the flows injected both free energy and magnetic helicity throughout the coronal volume interior to the separatrix, i.e., on all field lines that root at both ends within the northern hemisphere (red lines in Fig. 1b). Everywhere on the solar surface outside of the minority polarity, the magnetic field was line-tied at rest ($\mathbf{V}_\perp = 0$) at all times during the simulation. Hence, any changes in the connectivity of field lines outside of the initial separatrix dome occurred solely due to reconnection in the corona. Both reconnection and convection contributed to connectivity changes inside the dome. Except for the localized dynamics due to reconnection, the pre-eruption evolution was approximately quasi-static, as in the real corona, because the average photospheric driving speed ($\approx 25 \text{ km s}^{-1}$) was much smaller than the typical Alfvén speed in the bipolar active region ($\approx 1,000 \text{ km s}^{-1}$).

3. RESULTS

In this section, we present the results of our simulation, tracing the evolution of the system through the self-consistent formation of the filament channel (§3.1) to its eventual explosive eruption in a CME (§3.2). We then examine in detail the timings of impulsive flare-reconnection onset and kinetic- and magnetic-energy changes (§3.3) and the topological evolution of the magnetic field (§3.4).

3.1. Energy Buildup

The formation of the filament channel is shown in Figure 1 at times early ($t = 1,000$ s, when the vortical flows attain their peak speed) and late in the evolution, ($t = 80,000$ s, not long before onset of eruption). Panels d,f show the shear component of the magnetic field, B_ϕ , color-shaded against the sky at the central meridian ($\phi = 0$). The alternating red and blue contours in Figure 1d mark the weakly twisted structures generated initially by the individual vortical cells. Over time, these alternating bands of shear field strengthen and reconnect with their neighbors, transporting the shear flux toward the outer boundary of the minority-polarity region, i.e., the PIL. Figure 1f shows the resulting concentration into a localized region above the PIL, consistent with previous modeling of helicity condensation (e.g., cf. Fig. 4 in Knizhnik et al. 2015). The three-dimensional filament channel penetrates the meridional plane twice, yielding two oppositely signed regions of B_ϕ . Viewed from above in Figure 1e, the channel is seen to be quasi-circular and to envelope the whole PIL. It consists of an arcade of highly sheared, low-lying flux (orange) beneath weakly sheared, high-lying flux (red, above the southern segment of the PIL).

A key point is that the simple driver of our system consists solely of small-scale, compact, close-packed, vortical flows. If the system evolution were purely ideal, these flows would never produce the global-scale filament channel evident in Figure 1. The combination of the flows with helicity-conserving coronal magnetic reconnection, however, produces a very highly sheared filament channel whose properties are consistent with solar observations. As Figure 1f indicates, the resulting self-organized structure consists of a balance of forces between an outward magnetic pressure exerted by the out-of-plane field component and an inward magnetic tension exerted by the stretched in-plane field components. We discuss below how this force balance is disrupted.

3.2. Eruption

The buildup of the filament channel shown in Figure 1 strongly perturbs the overlying magnetic field and sets the stage for the later eruption. As shown in Figure 2, between times $t = 0$ (a) and $t = 59,500$ s (b), the expansion of the separatrix dome moves the coronal magnetic null point outward and slightly equatorward. This motion also compresses the null to form a current sheet, which allows slow magnetic-breakout reconnection to begin there. Evidence for this can be seen in Figure 2b: the two innermost green field lines that initially connected into the southern hemisphere now connect into the minority-polarity region in the north. This has removed flux that overlay the separatrix dome and the southern portion of the PIL by transferring it to overlie the northern portion of the PIL, weakening the restraining tension force above the dome and enabling further expansion. Additional evidence of breakout reconnection is shown by the orange field lines, which now connect to the southern hemisphere rather than into the minority-polarity region in the north as they did previously.

By time $t = 89,000$ s in Figure 2c, the eruption is well underway. All but two of the green field lines now connect into the minority-polarity region and no longer overlie the southern portion of the PIL, where a section of the strongly sheared filament channel (bundle of orange field lines) is erupting outward at high speed, $v_r > 1,000$ km s⁻¹ (dark red shading). At time $t = 90,000$ s in Figure 2d, the ejected sheared flux has more than doubled its height above the surface, and reconnection has commenced below where the fluxes from each side have closed back together in the wake of the CME. This is evidenced by the green field lines that have reestablished their connections to the southern hemisphere at this time. Paired upflows (red) and downflows (blue) highlight the flare reconnection jets beneath the high-speed ejecta.

The flare reconnection not only restores all of the green field lines to their original connections to the southern hemisphere, as seen in Figure 2e, but also creates entirely new connections of blue field lines to the southern hemisphere, whereas previously they connected only into the minority polarity in the north. This process weakens the field overlying the northern portion of the PIL, so now that segment of the sheared filament channel also erupts at high speed in a “sympathetic” ejection. (The orange sheared field lines that are drawn participate only in the first eruption, not the second.) This second eruption is deflected equatorward by the overlying field, as can be seen at time $t = 93,000$ s in Figure 2f. The flare reconnection jets below the second CME also are clearly visible in this image. Therefore, although the eruptive event begins in the filament channel above the southern portion of the PIL, it eventually encompasses the entire channel and PIL encircling the minority-polarity region.

3.3. Energetics and Timings

To clarify the mechanism for eruption onset, we display the global energetics and other properties of our simulation in Figure 3. Full time histories of the total, volume-integrated magnetic (U_M ; black curve) and kinetic (U_K ; blue curve) energies are shown in Figure 3a. Filament-channel formation occurs up to time $t \approx 88,300$ s, marked by the vertical dashed line in the plot, when the eruption begins. During the formation phase, the vortical surface driving builds up the free magnetic energy at a nearly constant rate, until this energy eventually reaches $U_M \approx 6 \times 10^{32}$ erg, which is about 20% of the initial potential-field energy. After a brief startup phase, the kinetic energy U_K exhibits two extended intervals of quasi-steady values: $\approx 2 \times 10^{29}$ erg early, and $\approx 5 \times 10^{29}$ erg later, with a transition occurring between $t \approx 50,000$ s and $t \approx 60,000$ s. This transition coincides with the onset of breakout reconnection in the corona, as discussed and illustrated in the preceding §3.2 and Figure 2. The early behavior is associated primarily with the imposed vortical flows and the pervasive reconnection outflows that follow from the helicity-condensation process; the late evolution has an additional kinetic-energy contribution due to the slow outward expansion of the filament channel and the overlying separatrix dome, along with some reconnection outflows near the null point. All of this flow energy remains small, amounting to only about 0.1% of the stored magnetic free energy, during the buildup phase.

Also shown in Figure 3a is the maximum longitudinal field strength (B_ϕ^{\max} ; red curve) within the computational domain. This quantity provides an approximate measure of the maximum magnitude of the shear field in the filament

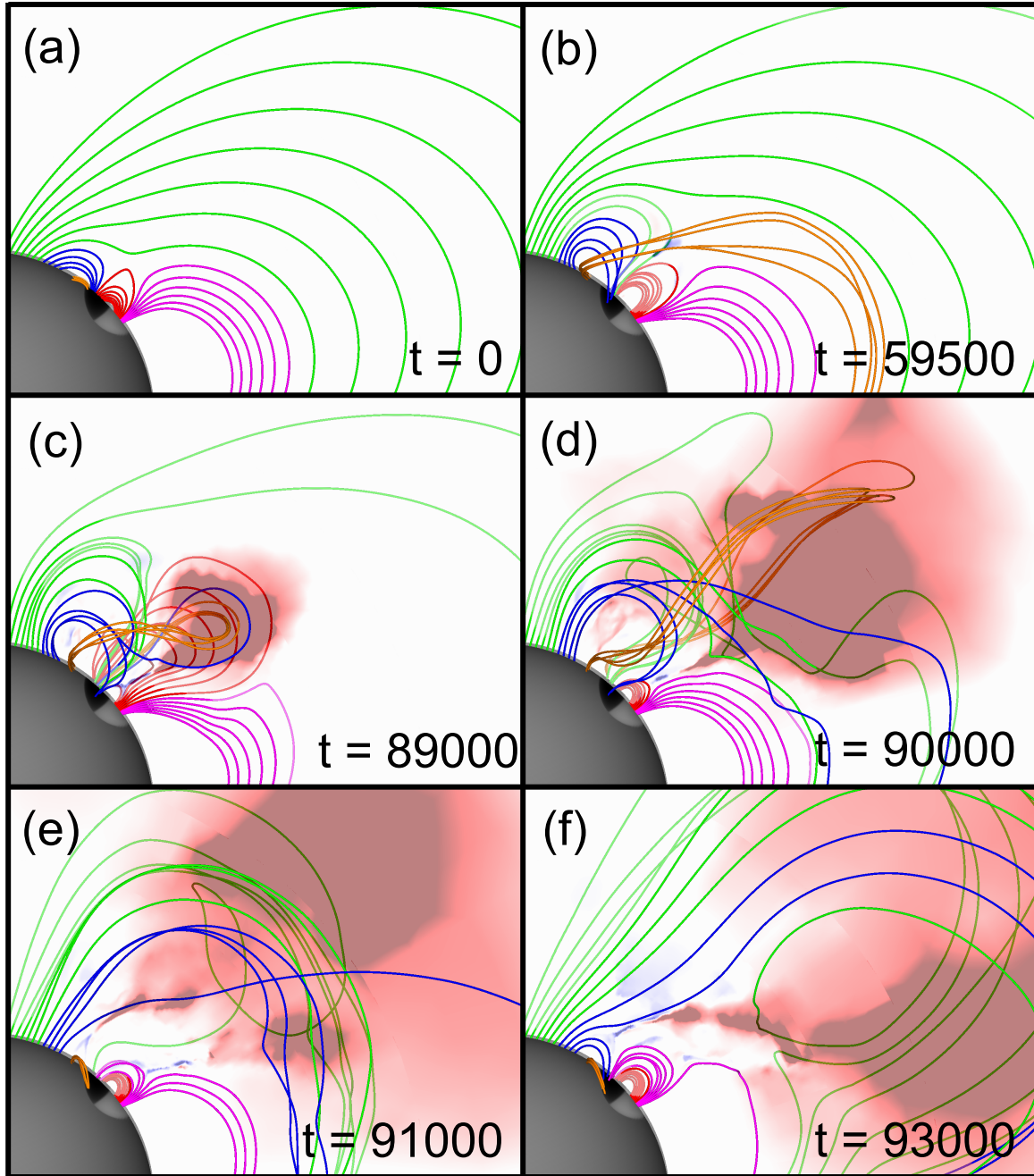


Figure 2. Filament-channel eruption. Surface shading and magnetic field-line coloring are the same as in Figure 1. Red (blue) shading in the semi-transparent plane at $\phi = 0$ shows outward (inward) radial flow saturated at $\pm 1,000 \text{ km s}^{-1}$. An animation is available. The video starts at $t = 86600$ and ends at $t = 99100$. Its duration is 15 seconds.

channel. The initial value in the potential field is about 30 G. As the vortical surface driving twists the magnetic field lines within the minority-polarity region, the maximum strength increases, peaking at about 70 G at time $t \approx 20,000$ s. Thereafter, although the amount of shear flux continues to increase as the helicity condenses to build the filament channel, the upward expansion increases the cross-sectional area of the channel fast enough that the strength of the shear field declines. This result is expected from the classic arguments of the Aly-Sturrock free-energy limit (Aly 1991, Sturrock 1991). We note that there is a subtle, but perceptible, steepening of the slope of the B_{ϕ}^{\max} curve simultaneous with the increase in kinetic energy, associated with the onset of slow breakout reconnection as noted above.

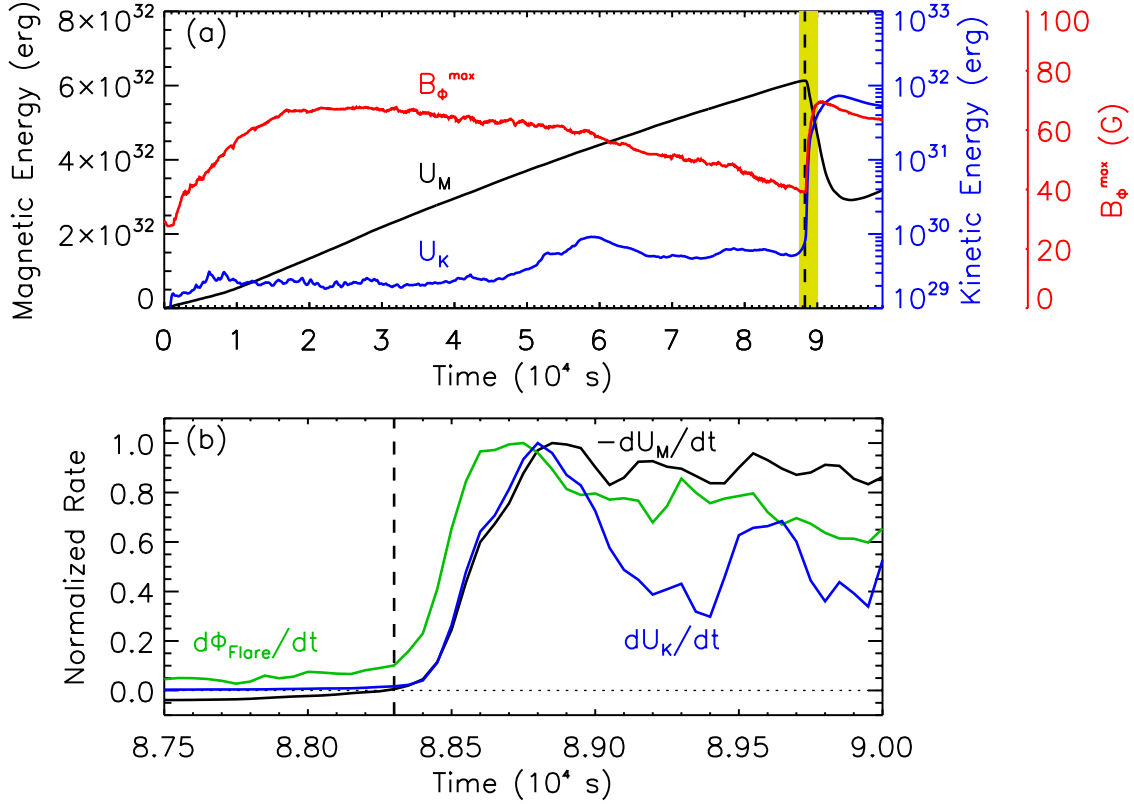


Figure 3. Global energetics. (a) Time histories of total magnetic (U_M) and kinetic (U_K) energies and of maximum longitudinal field strength (B_ϕ^{\max}); the yellow-shaded region is the temporal interval expanded in the bottom panel. (b) Rates of change of total magnetic and kinetic energies and of flare-reconnected flux, normalized to their respective peak values ($dU_M/dt = 1.1 \times 10^{29}$ erg s $^{-1}$; $dU_K/dt = 4.4 \times 10^{28}$ erg s $^{-1}$; $d\Phi_{\text{Flare}}/dt = 5.5 \times 10^{18}$ Mx s $^{-1}$), around the time of eruption onset marked by the dashed vertical line in both panels.

The initiation of the filament-channel eruption at $t \approx 88,300$ s (dashed line) in Figure 3a is accompanied by steep changes in all three quantities. The kinetic energy rises by more than two orders of magnitude, reaching a large fraction (about 10%) of the total stored magnetic free energy. This indicates a sudden transition from very low-speed flows to very high-speed flows, whose average Alfvén Mach number is about 0.2. The maximum longitudinal field strength nearly doubles very quickly as the shear flux below the eruption is compressed by the downward contracting flare loops (e.g., Zucarello et al 2017). Energy is extracted from the magnetic field to power the high-speed flows and the local B_ϕ compression, as indicated by the approximately 50% drop in magnetic energy during the eruption.

In order to understand in more detail the transition from channel formation to eruption, we expanded the small interval indicated by the yellow shading in Figure 3a for display in Figure 3b. There we show the rates of change of the total magnetic (dU_M/dt ; black) and kinetic (dU_K/dt ; blue) energies, along with that of the total flare-reconnected flux $d\Phi_{\text{flare}}/dt$; green), which we measured by tracking discontinuous changes in the lengths of magnetic field lines rooted in the minority-polarity region. This plot shows that strong flare reconnection begins first, and is followed by initiation of the rise in kinetic energy simultaneous with the decline in magnetic energy. This sequence demonstrates conclusively that reconnection plays the primary role in initiating the explosive eruption of the filament channel, and is fully consistent with previous work on magnetic breakout for both CMEs/EFs (Karpen et al. 2012) and coronal jets (Wyper et al. 2017, 2018).

3.4. Topological Evolution

The reconnection dynamics that accompany the filament-channel formation and eruption are illuminated by examining the topological evolution of the system in Figure 4. Figure 4a depicts the initial magnetic connectivity. The solid-shaded medium blue region in the north maps to the southern hemisphere (diagonal dark blue shading), while the

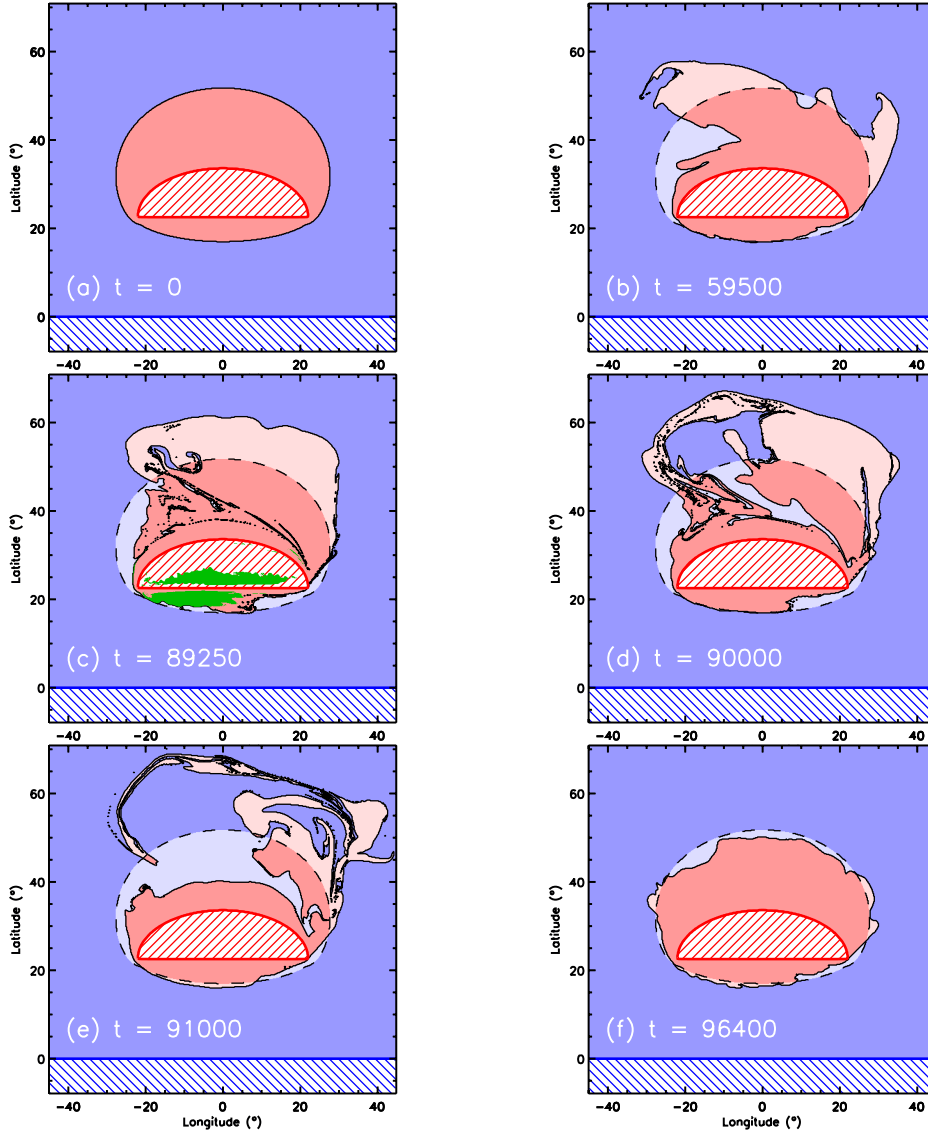


Figure 4. Connectivity maps at six steps in the evolution. Dark red/blue shading with diagonal lines indicates minority-polarity flux in the northern hemisphere and all flux in the southern hemisphere, respectively. Medium red/blue shading indicates flux that closes to the northern/southern hemisphere. Light red/blue shading indicates flux that closes to the northern/southern hemisphere that initially connected to the opposite hemisphere. Solid black lines mark the intersection of the separatrix surface with the photosphere; dashed black lines mark the initial location of this intersection. Green shading in (c) indicates flux that has undergone flare reconnection. An animation is available. The video starts at $t = 0$ and ends at $t = 96400$. Its duration is 15 seconds.

solid-shaded medium red region in the north maps to the minority-polarity flux in the active region (diagonal dark red shading). The black contour is the intersection of the separatrix dome, which encloses all of the flux connecting to the minority-polarity region, with the solar surface. All field lines outside of the minority-polarity region are line-tied and fixed ($\mathbf{v}_\perp = 0$), and only those lines are used to compute the connectivity maps. Hence, all changes in the connectivity shown in Figure 4 occur due to reconnection.

As the minority-polarity flux is twisted by the vortical motions and then accumulates concentrated shear via helicity condensation, magnetic pressure builds up within the separatrix dome and deforms the coronal null to form a current sheet. Over time, the resulting reconnection changes the connectivity of the flux at the solar surface. By time $t = 59,000$ s, some of the majority-polarity flux that initially closed within the separatrix dome (medium red, Fig. 4a) has reconnected and now closes to the southern hemisphere (light blue, Fig. 4b). Correspondingly, an equal amount

of the majority-polarity flux that initially closed to the southern hemisphere (medium blue, Fig. 4a) now closes to the minority-polarity region (light red, Fig. 4b). Thus, the breakout reconnection has the effect of transferring the flux that overlies the southern segment of the PIL (the straight portion of the dark red minority-polarity boundary) so that it overlies the northern segment (the curved portion of that boundary).

This process continues and expands the area of changed connectivity until the flux overlying the southern segment of the PIL weakens sufficiently to allow eruption to occur. Figure 4c shows the topology at $t = 89,250$ s, shortly after flare-reconnection onset and initiation of the eruption above the southern segment of the PIL (Fig. 2c). Additional flux has been removed from above the southern segment of the PIL (see in particular the light blue regions in the southern half of the active region, where a small area corresponds to a comparatively large amount of flux due to the high field strength). The flux that has undergone closed-closed flare reconnection within the separatrix dome is shown in green. This region corresponds to the classic flare ribbons. It maps out a region along the southern segment of the PIL and, due to the shear concentrated there, the kernel of reconnected flux south of the PIL is displaced to the east. We note also that the separatrix boundary has become highly fragmented and fractal in character, possessing structure down to the grid scale.

As the eruption proceeds, the connectivity continues to evolve in structure and complexity. Subsequent maps are shown at times $t = 90,000$ s and $91,000$ s in Figures 4d,e for comparison with the preceding Figures 2d,e. As the flare reconnection progressively processes flux in the green and blue flux systems drawn in Figure 2 at these times, the connectivity of the field lines switches from the minority-polarity region in the northern hemisphere to the southern hemisphere. This change is indicated by the new light blue regions adjacent to the northern separatrix boundary in Figure 4, especially at the later time (Fig. 4e). The strong reduction in the flux overlying the northern segment of the PIL enables that section of the filament channel to erupt, as we noted above in §3.3. In the wake of that secondary ejection, flare reconnection above the northern segment of the PIL then acts to restore the connections of the blue field lines from the southern hemisphere back to the north, as shown in Figures 2e,f. This is reflected in the change in the connectivity-map colors from light blue to medium red in Figures 4e,f.

After the conclusion of the two episodes of CME ejection and flare reconnection, above first the southern and then the northern segments of the PIL, the system contains subcritical amounts of helicity and magnetic free energy and relaxes toward a new equilibrium state. The connectivity at the end of the simulation is shown in Figure 4f. The separatrix dome has taken on a configuration that rather closely resembles the initial state, and all of the connectivity changes at this time are localized near the original separatrix boundary. Ongoing helicity condensation now can rebuild the free energy and helicity in the channel until it once again attains the critical condition for a new eruption.

4. DISCUSSION

This article presents the first calculations of a CME powered by self-consistent energy buildup via helicity condensation. We have shown that a coronal field configuration driven by helicity-injecting flows leads to a stressed magnetic structure consistent with observations and that this structure eventually erupts explosively. Breakout reconnection above destabilizes the system, and the onset of flare reconnection below produces explosive CME acceleration and rapid magnetic energy release, generating and ejecting a flux rope.

The eruption phases discussed in §3.3 are largely consistent with the results of prior high-resolution 2.5D studies (Karpen et al. 2012). However, several new aspects arise due to the three-dimensional topology. The PIL in these calculations is semicircular, rather than an axisymmetric line. Viewed from the mid-plane (as in Fig. 1f), it can be seen that the two locations for shear accumulation and magnetic pressure stress the null point in orthogonal directions, inhibiting its deformation into a current sheet. This allows more energy to build up prior to eruption, explaining why the maximum free energy ($\approx 21\%$) is substantially larger than in 2.5D simulations ($\approx 11\%$). The entire filament channel is ejected; the southern half erupts first and the northern half follows “sympathetically,” as is frequently observed.

Another consequence of the three-dimensional configuration is a rotational asymmetry in the breakout reconnection (see in particular Fig. 4). Due to the large-scale twist in the field inside the separatrix dome, when the flux above the southern half of the PIL undergoes breakout reconnection, the resulting reconfigured flux is positioned on the east of the minority polarity. The overlying field accumulates more shear compared to prior studies of the helicity condensation process (cf. Fig. 3 in Knizhnik et al. 2017b). This may be because only six cellular flows span the narrowest part of the minority polarity; on the other hand, observations of coronal cells indicate that the magnetic-shear region extends a substantial distance from the filament channel (N. R. Sheeley et al. 2013).

The primary conclusion from our calculation is that a broad variety of solar features, both pre- and post-eruption, follow directly from a turbulent-like inverse cascade of magnetic helicity in a simple multipolar topology. These ingredients are ubiquitous in the solar corona. In this Study, we assumed a set of uniform rotational surface flows for simplicity; however, the particular form of the driving should not be important, so long as there is a net injection of helicity and sufficiently complex flows to drive the pervasive reconnection required for the cascade. Net helicity may be injected into the corona in other ways, such as through both flux emergence and cancellation, as well as by large-scale flows as in active-region rotation. Regardless of the source of the injected helicity, stochastic coronal reconnection will concentrate structure at PILs and inevitably lead to explosive eruption.

Our work was supported by NASA's LWS, H-SR, H-ISFM, and HEC research programs. Joel Dahlin acknowledges support from the NASA LWS Jack Eddy Fellowship administered by the University Corporation for Atmospheric Research. Joel Dahlin's research was also supported by an appointment to the NASA Postdoctoral Program at the NASA Goddard Space Flight Center, administered by Universities Space Research Association under contract with NASA. We also acknowledge use of Peter Wyper's magnetic-topology tools to generate Figure 4.

REFERENCES

- Antiochos, S. K. 1990, *MmSAI*, 61, 369
- . 1998, *ApJL*, 502, L181
- . 2013, *ApJ*, 772, 72
- Antiochos, S. K., DeVore, C. R., & Klimchuk, J. A. 1999, *ApJ*, 510, 485
- Berger, M. A. 1984, *GApFD*, 30, 79
- Berger, M. A., & Field, G. B. 1984, *JFM*, 147, 133
- DeVore, C. R., & Antiochos, S. K. 2008, *ApJ*, 680, 740
- Fan, Y. 2001, *ApJL*, 554, L111
- Finn, J. M., & Antonsen, T. M. 1985, *CoPPC*, 9, 111
- Forbes, T. G., Linker, J. A., Chen, J., et al. 2006, *SSRv*, 123, 251
- Gaizauskas, V. 1998, in *New Perspectives on Solar Prominences*, ed. D. F. Webb, B. Schmieder, & D. M. Rust (San Francisco: ASP), 257–264
- Karpen, J. T., Antiochos, S. K., & DeVore, C. R. 2012, *ApJ*, 760, 81
- Kliem, B., & Török, T. 2006, *PhRvL*, 96, 255002
- Knizhnik, K. J., Antiochos, S. K., & DeVore, C. R. 2015, *ApJ*, 809, 137
- . 2017a, *ApJ*, 835, 85
- Knizhnik, K. J., Antiochos, S. K., DeVore, C. R., & Wyper, P. F. 2017b, *ApJL*, 851, L17
- Knizhnik, K. J., Uritsky, V. M., Klimchuk, J. A., & DeVore, C. R. 2018, *ApJ*, 853, 82
- Lau, Y.-T., & Finn, J. M. 1990, *ApJ*, 350, 672
- Linker, J. A., Mikić, Z., Lionello, R., et al. 2003, *PhPl*, 10, 1971
- Lynch, B. J., Antiochos, S. K., DeVore, C. R., Luhmann, J. G., & Zurbuchen, T. H. 2008, *ApJ*, 683, 1192
- Lynch, B. J., Antiochos, S. K., Li, Y., Luhmann, J. G., & DeVore, C. R. 2009, *ApJ*, 697, 1918
- Lynch, B. J., Masson, S., Li, Y., et al. 2016, *JGRA*, 121, 10
- Mackay, D. H., DeVore, C. R., & Antiochos, S. K. 2014, *ApJ*, 784, 164
- Mackay, D. H., DeVore, C. R., Antiochos, S. K., & Yeates, A. R. 2018, *ApJ*, 869, 62
- Martin, S. F. 1998, *SoPh*, 182, 107
- Masson, S., Antiochos, S. K., & DeVore, C. R. 2013, *ApJ*, 771, 82
- Moore, R. L., Sterling, A. C., Hudson, H. S., & Lemen, J. R. 2001, *ApJ*, 552, 833
- N. R. Sheeley, J., Martin, S. F., Panasenco, O., & Warren, H. P. 2013, *ApJ*, 772, 88
- Priest, E. R., & Titov, V. S. 1996, *RSPSA*, 354, 2951
- Wyper, P. F., Antiochos, S. K., & DeVore, C. R. 2017, *Natur*, 544, 452
- Wyper, P. F., DeVore, C. R., & Antiochos, S. K. 2018, *ApJ*, 852, 98
- Zhao, L., DeVore, C. R., Antiochos, S. K., & Zurbuchen, T. H. 2015, *ApJ*, 805, 61